

Comprehensive Investigation of Fundamental Mode Profiles in Monolithic Nonplanar Ring Oscillators

WEITONG FAN[†], CHUNZHAO MA[†], WENXUN LI, DANQING LIU, ZELONG HUANG, JIE XU, CHANGLEI GUO*, AND HSIEN-CHI YEH

MOE Key Laboratory of TianQin Mission, TianQin Research Center for Gravitational Physics & School of Physics and Astronomy, Frontiers Science Center for TianQin, CNSA Research Center for Gravitational Waves, Sun Yat-sen University (Zhuhai Campus), Zhuhai 519082, China

[†]*These authors contributed equally to this work.*

* guochlei@mail.sysu.edu.cn

Abstract: Nonplanar ring oscillators (NPROs) are building blocks for high-performance single-frequency lasers and ring-laser gyroscopes that have profoundly improved the state-of-the-art laser technologies, fundamental research and precision measurements. However, a comprehensive investigation of fundamental mode profiles in monolithic NPROs has been a missing part even though they will affect the performance of the lasers or ring-laser gyroscopes. Here, we present a comprehensive finite-element modeling of the output beam profiles of monolithic NPROs by combining ABCD transmission matrix and generalized Huygens-Fresnel integral. We theoretically investigate the effects of geometric parameters of monolithic NPROs on their output mode profiles. In particular, we focus on the thermal effect inside the monolithic NPRO and calculate the equivalent focal-length of the thermal-lens by using a ray-tracing-method. Furthermore, we experimentally characterize the output laser beam profile, reconstruct the beam profile at the A-facet of the monolithic NPRO, and compare the experimental results with the simulation, thereby validating the accuracy and reliability of our model. The investigation may facilitate monolithic NPRO design and subsequently improve the performances of NPRO lasers and gyroscopes in the future.

© 2025 Optica Publishing Group under the terms of the Optica Publishing Group Open Access Publishing Agreement

1. Introduction

The concept of nonplanar ring oscillators (NPROs) based on Nd:YAG was first proposed by A.R. Clobes in 1972 [1]. Exploiting the Sagnac effect, the NPRO laser has also been successfully employed as ring-laser gyroscopes for rotational sensing [2–5]. With the continuous advancement of laser technology, the monolithic nonplanar ring oscillator was reported by Kane in 1985 [6]. This innovative design integrates the gain medium and the resonator into a single unit, establishing itself as a high-performance laser that has been widely utilized in industrial, scientific, and space missions to the present day [7–13]. Recent report has validated the application of monolithic NPRO in laser gyroscope, demonstrating the significant potential of this type of NPRO for use in gyroscopic applications [14]. In both fields of single-frequency lasers and ring-laser gyroscopes, the shapes of output fundamental mode profiles from NPRO lasers are of utmost importance, because a pure Gaussian beam is preferred for many applications. In precision measurements like gravitational wave detection, the interference highly relies on the injection of the fundamental transverse mode into the interferometer [15–17]. Thus, ensuring the mode purity of the laser output and the beam quality of the fundamental mode are crucial. Moreover, the mode profiles are also strongly correlated with thermal effects in the resonator, where the latter is crucial for laser design especially for

optical power scaling [18–23]. Therefore, a comprehensive investigation of fundamental mode profiles in monolithic NPROs is very necessary.

In previous studies on NPROs [24–26], methods have been established for calculating the output beam profiles. However, these methods are primarily applicable under the conditions of large resonator using discrete optics, as well as in equilateral ring configurations (pertain to large-scale laser gyroscopes). Such approaches are not suitable for smaller, non-equilateral monolithic NPROs. Furthermore, the thermal field induced by pump lasers can significantly affect the output beam profiles, yet this aspect has not been thoroughly addressed in previous studies [27–30]. Although the thermal-lens effects in monolithic NPROs have been studied [31], the focal lengths obtained through integral calculations remain insufficiently intuitive, and there has been no experimental validation to support their findings. To date, there has been still a lack of reports addressing the output beam profiles of widely utilized monolithic NPRO, particularly studies that encompass various sizes and design configurations, as well as the alterations in the beam profiles induced by thermal-lensing effects at different pump levels. Thus, a gap remains between a complete knowledge of monolithic NPRO mode profile and its more and more profound applications in high-performance laser technologies.

In this work, we present a comprehensive study on the output beam profiles of monolithic NPROs with a more flexible calculation method. We systematically investigate the effects of various geometrical parameters, including the out-of-plane angle, incident and output laser angles, and the dimensions, on the spatial distribution of the output beam profiles using finite-element method (FEM). Furthermore, we place significant emphasis on the effects of thermal-lens within the monolithic NPRO. We calculate the equivalent focal length of the thermal-lens through physical field simulations and ray-tracing-method, presenting a more intuitive physical result and analyze the impact of thermal-lens on the output beam profile, which is further validated by experimental results. The results of this work can optimize the design of monolithic NPROs used for single-frequency lasers and gyroscopes [14,32–34].

2. ABCD Matrix of beam transmission in monolithic NPRO

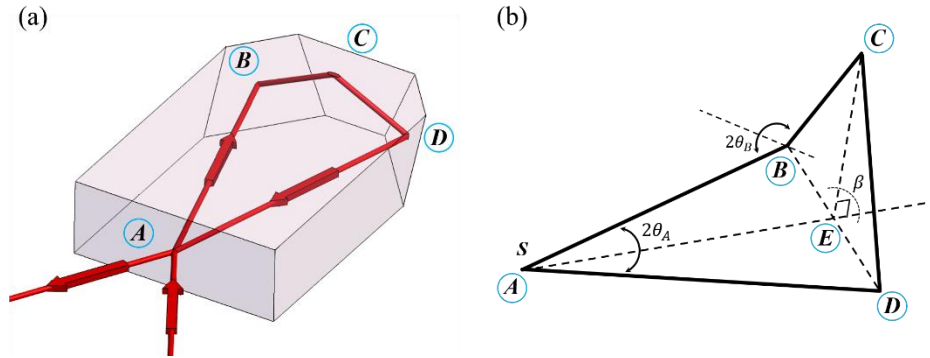


Fig. 1. (a) The structure and optical path of monolithic NPRO. Red traces mark the optical path along $A-B-C-D-A$. (b) The geometric structure of the light path in monolithic NPRO. AE , CE and BD are auxiliary lines for the nonplanar ring, and E is the midpoint of BD . θ_A , θ_B and β are also defined here.

Fig. 1(a) illustrates the schematic structure of a typical monolithic NPRO, which consists of one output coupling facet and three total internal reflection (TIR) facets. Point A is located at front facet, which is coated for anti-reflection at pump wavelength and high-reflection at laser wavelength. The facets containing points B , C , and D are optically polished planes where total internal reflection occurs. The geometric structure of the light path within the resonator is shown in Fig. 1(b), defined by four non-coplanar reflective facets, where β is the dihedral angle between the two transmission planes. θ_A and θ_B are half the angle between the incident and reflected beams. Point E is the midpoint of the BD connection. We assume that the beam

within the resonator originates from point S which is on leg AB and infinitely close to point A , propagating in a clockwise direction along the $A-B-C-D-A$ path.

Fig. 2 demonstrates the coordinate transformations among different main axis systems. During one round trip within the resonator, the beam undergoes four reflections, and the nonplanar characteristics of the resonator result in the incident planes of successive reflections being non-coplanar. Therefore, it is necessary to describe both the incident and reflected waves in the main axis system, where the vector z aligns with the direction of beam propagation, vector y lies within the transmission plane and is orthogonal to z , and vector x is determined by the right-hand rule. The beam propagating along AB reflects at point B , resulting in a rotational transformation of the vectors between the incident and reflected coordinate systems. The vectors x, y, z will first undergo reflection transformations, with y_{AB} transitioning to y'_{AB} , while the vector z continues along the direction of the reflected beam.

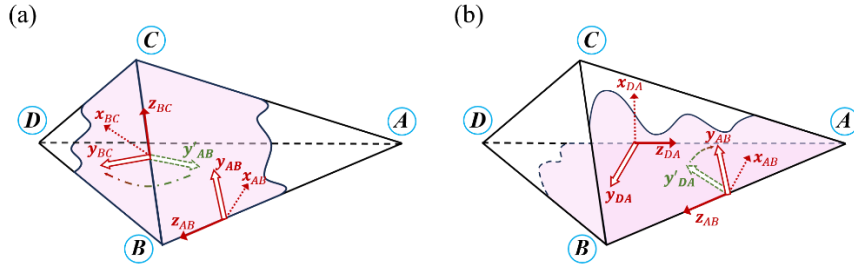


Fig. 2. The coordinate transformations among different main axis systems. (a) From leg AB to BC ; (b) From leg DA to AB . The x, y, z vectors are used to define the direction of beam propagation and spatial coordinate changes. The pink area represents the plane where the light beam propagates.

To ensure that the description of the transmission loop strictly adheres to the new principal axis system, the x, y, z vectors will undergo another spatial coordinate rotation, maintaining the vector z along the direction of propagation, while the vector y adjusts to lie within the new transmission plane BCD (y_{BC}). The x vector is determined by the right-hand rule, perpendicular to the new transmission plane. Consequently, in the context of continuous mirror reflections involving different axis systems, it becomes necessary to introduce a rotation matrix that projects the vectors from the old coordinate system to the new one. The rotation matrix is expressed as Eq. (1).

$$M(\beta) = \begin{bmatrix} \cos(\beta) & -\sin(\beta) & 0 & 0 \\ \sin(\beta) & \cos(\beta) & 0 & 0 \\ 0 & 0 & \cos(\beta) & \sin(\beta) \\ 0 & 0 & -\sin(\beta) & \cos(\beta) \end{bmatrix} \quad (1)$$

In conventional resonator theory, paraxial beam would escape from cavities formed by four planar mirrors, preventing resonance. The NPRO, due to the existence of internal thermal-lens, constrain the paraxial beam and resonate. We equivalently represent the thermal-lens introduced by temperature-induced refractive index gradients in the beam loop as two concave lenses located at points A and B (detailed analysis will be conducted in Section. 4). Therefore, the reflection matrix Mr at points A and B can be replaced with a spherical mirror transformation matrix, as shown in Eq. (2), and f is the equivalent focal length of the thermal-lens. The placement of the spherical lens at point B is primarily intended to enhance the model's accuracy under high pump-power.

$$M(\theta) = \begin{bmatrix} 1 & 0 & 0 & 0 \\ 0 & 1 & 0 & 0 \\ -1/f / \cos(\theta) & 0 & 1 & 0 \\ 0 & -\cos(\theta) / f & 0 & 1 \end{bmatrix} \quad (2)$$

The free propagation matrix of the beam within the medium can be expressed as Eq. (3), where L is the length of the laser propagation and n is the refractive index of the gain medium.

$$M(L) = \begin{bmatrix} 1 & 0 & L/n & 0 \\ 0 & 1 & 0 & L/n \\ 0 & 0 & 1 & 0 \\ 0 & 0 & 0 & 1 \end{bmatrix} \quad (3)$$

Utilizing the ABCD matrix for beam propagation, we can derive the expression for the beam transmission loop after one round trip starting from point S within the resonator, as presented in Eq. (4).

$$\begin{aligned} M_{round} &= M(\beta_{D-AB-C})M(\theta_A)M(L_{AD})M(\beta_{C-AD-B})M_r M(L_{CD}) \\ &\quad M(\beta_{B-CD-A})M_r M(L_{BC})M(\beta_{A-BC-D})M(\theta_B)M(L_{AB}) \\ &= \begin{bmatrix} A_{2 \times 2} & B_{2 \times 2} \\ C_{2 \times 2} & D_{2 \times 2} \end{bmatrix} \end{aligned} \quad (4)$$

3. Transverse Profiles in monolithic NPRO

Combining the ABCD transmission matrix, the initial electric field E_1 originating from S and the profile E_2 after one-round-trip transmission can be theoretically studied by using the generalized Huygens-Fresnel integral, as shown in Eq. (5). Here, $r_i^T = (x_i, y_i)$, $i=1,2$, represents the transverse positions, where i denotes the respective fields.

$$\begin{aligned} E_2(x_2, y_2, z_{cycle}) &= \left(-\frac{i/\lambda}{|B|^{1/2}} \right) \exp(ikz) \iint dx_1 dy_1 E_1(x_1, y_1, 0) \\ &\quad \cdot \exp \left\{ \frac{ik}{2} \begin{bmatrix} r_1 \\ r_2 \end{bmatrix}^T \begin{bmatrix} B^{-1}A & -B^{-1} \\ -B^{-1} & DB^{-1} \end{bmatrix} \begin{bmatrix} r_1 \\ r_2 \end{bmatrix} \right\} \end{aligned} \quad (5)$$

According to the self-reproducing mode principle, certain optical beam within a resonator, after propagating through the cavity and returning to their initial position, maintain the same spatial distribution of optical field as when it originates. This leads to the following expression (6), where γ represents the amplitude decay and phase change.

$$E_2(x_2, y_2, z) = \gamma E_1(x_1, y_1, 0) \quad (6)$$

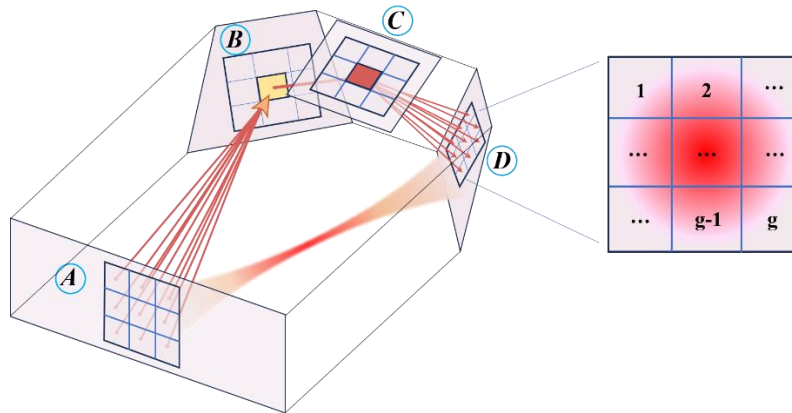


Fig. 3. Discretization of the four facets of monolithic NPRO. In subsequent calculations, each facet with dimensions of $330 \mu\text{m} \times 330 \mu\text{m}$ will be divided into 33^2 smaller units in a square configuration ($g=33^2$).

Since it is not feasible to obtain an analytical solution by directly solving Eqs. (5) and (6), we resort to the FEM for analysis. We discretize the four facets of the monolithic NPRO, as illustrated in Fig. 3. During the meshing process, we observe that each element on one mirror interacts with every element on the subsequent mirror, and similarly, all elements on one mirror will influence each element on the next mirror [35]. Consequently, the electric field E_1 can be represented by $E_1 = [e_1, e_2, e_3, \dots, e_g]^T$, where g represents the total number of discretized elements. Additionally, each small element e_j corresponds to different position, represented by $r_{ij}^T = (x_{ij}, y_{ij})$ with $i = 1, 2$ and $j = 1 \sim g$.

The amplitude within each element can be considered as invariant when the number of discretized elements is sufficiently large, thus allowing us to express E_1 in Eq. (5) independent of the variations in the integration variables x and y . Therefore, we can rewrite Eq. (5) as the following Eq. (8). The eigenvectors of matrix V characterize the complex electric field at the position S , while the eigenvalues represent the corresponding mode losses.

$$\gamma \begin{bmatrix} e_1 \\ e_2 \\ \vdots \\ e_g \end{bmatrix} = V \times \begin{bmatrix} e_1 \\ e_2 \\ \vdots \\ e_g \end{bmatrix}, \quad V = \begin{bmatrix} v_{11} & v_{12} & \cdots & \cdots & v_{1g} \\ v_{21} & \ddots & & & \vdots \\ \vdots & & v_{jj'} & & \vdots \\ \vdots & & & \ddots & \vdots \\ v_{g1} & \cdots & \cdots & \cdots & v_{gg} \end{bmatrix}, \quad (j, j' = 1 \sim g) \quad (7)$$

$$v_{jj'} = \left(-\frac{i/\lambda}{|B|^{1/2}} \right) \exp(ikz) \iint dx_1 dy_1 \cdot \exp \left\{ \frac{ik}{2} \begin{bmatrix} r_{1j} \\ r_{2j'} \end{bmatrix}^T \begin{bmatrix} B^{-1}A & -B^{-1} \\ -B^{-1} & DB^{-1} \end{bmatrix} \begin{bmatrix} r_{1j} \\ r_{2j'} \end{bmatrix} \right\} \quad (8)$$

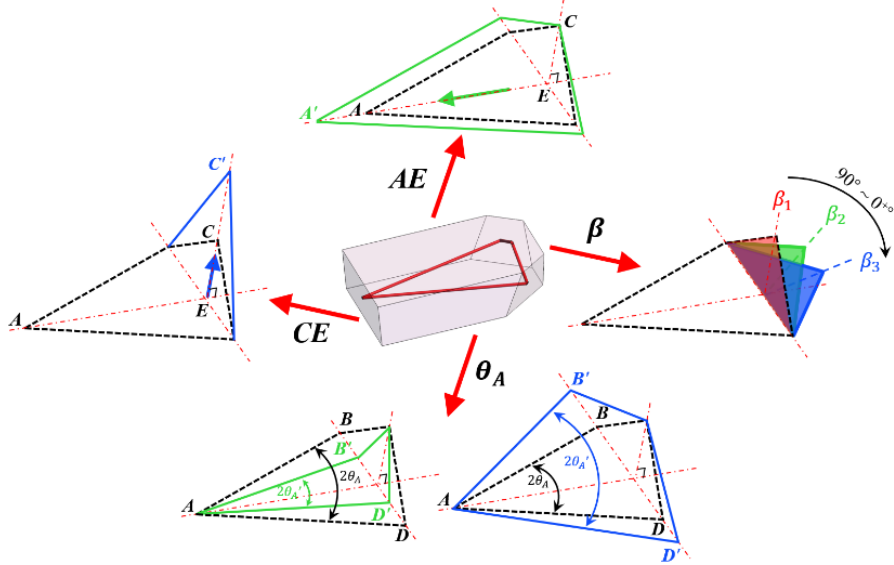


Fig. 4. Diagrams to show how the four critical parameters (AE , CE , β and θ_A) determine the geometry of monolithic NPROs.

Typically, the geometrical parameters of NPROs are primarily controlled by four independent variables: AE , CE , θ_A , and β , as shown in Fig. 4. AE and θ_A jointly determine the length of optical path within the resonator, while CE and the out-of-plane angle β define the height of the resonator. In the subsequent calculations, we will use the monolithic Nd:YAG (0.8 at.%) NPRO (3mm×8mm×12mm) employed in experiments as a reference, specifically with parameters $AE=10.5$ mm, $CE=1.5$ mm, $\theta_A=15^\circ$, $\beta=90^\circ$ (with coating of 99.8% for S-polarization and 94% for P-polarization), to analyze the variations with different design parameters.

By maintaining the length of AE or CE , while systematically varying the length of CE or AE , the beam profile at point S undergoes the changes as depicted in Fig. 5(a, b). The radius of the beam profile is shown by the red dashed line ($1/e^2$ of Gaussian fit). It can be observed that as CE progressively decreases, the beam radius correspondingly diminishes. Notably, when the ratio $AE:CE \geq 6$, the beam field's radius decreases slowly to a constant. This phenomenon occurs due to the fact that separation between the two concave lenses remaining constant. Contrary to the changing CE , the output beam profile does not exhibit a tendency towards a constant with the changing AE . This can be simply understood as the thermal-lens in the ring cavity being effectively located at points A and B . Changing the length of AE essentially modifies the distance between these lenses, thereby impacting the size of the output beam. The beam profile radius with changing AE (red curve) and CE (blue curve) are shown in Fig. 5(c).

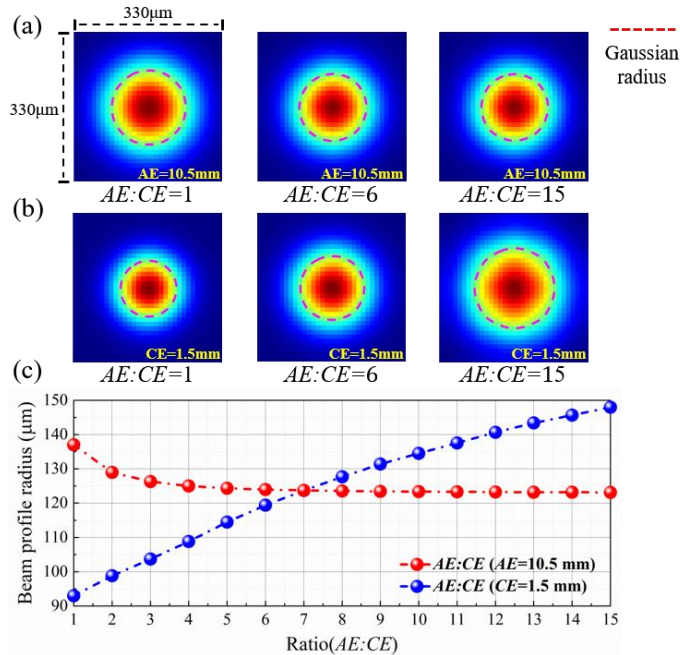


Fig.5. (a) The beam profiles at point S (see Fig. 1(b)) with different length of CE . (b) The beam profiles at point S with different length of AE . (c) Beam profile radius versus ratio of AE to CE . In the simulations, $\beta=90^\circ$, $\theta_A=15^\circ$, $f_A=4$ m, $f_B=10^5$ m

By varying the incident angle θ_A (with values selected near the boundaries of 0° to 90° , specifically 1° and 89°), the results are presented in Fig. 6(a). It can be seen that as the incident angle increases, the asymmetry of beam profile increases, and the laser beam field distorts finally. This distortion is due to the inclined mirrors with different curvature radii within the NPRO. The ellipticity of the output beam profile is defined as the ratio between the major and minor axes of the beam, as illustrated in Fig. 6(b). The combined effects of mirror curvature

variations and angular inclination cause asymmetric aberrations in the meridional and sagittal planes, leading to an asymmetric output beam. Our simulations show that when the incident angle θ_A exceeds 30° , this asymmetry becomes more pronounced. This issue can significantly affect coupling efficiency if the laser output from the NPRO is intended for fiber coupling.

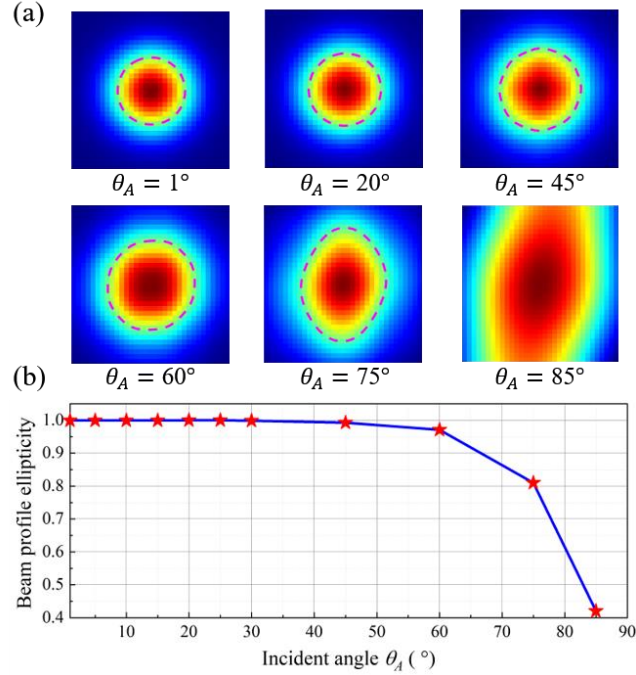


Fig. 6. (a) The beam profiles at point S with different incident angle θ_A . (b) Beam profile ellipticity versus incident angle. In the simulations, $AE=10.5$ mm, $CE=1.5$ mm, $\beta=90^\circ$, $f_A=4$ m, $f_b=10^5$ m.

In our theoretical calculations, we found that the out-of-plane angle of NPRO does not affect the output beam profile. However, previous studies have indicated that it influences the efficiency of magnetic field utilization along the beam path. Specifically, under the same magnetic field conditions, different out-of-plane angles result in varying loss differences between the clockwise and counterclockwise paths. The smaller is the out-of-plane angle, the lower is the required mode-selection magnetic-field strength.

4. Effects of Thermal-Lens on Beam Profile

In monolithic NPRO, thermal-lens effect arises primarily due to the absorption of pump laser by the gain medium within the cavity, which leads to localized heating (especially at the A -facet). This heating causes a change in the refractive index of the medium, creating a lens-like effect that can alter the path and focus of the laser beam. This phenomenon can significantly impact the performance and stability of the laser system, and has an influence on beam quality and alignment.

In the steady-state scenario, the internal temperature T distribution of the monolithic NPRO can be derived by solving the heat conduction equation. Within the Cartesian coordinate framework, the heat conduction equation for the resonator is formulated as Eq. (9), with the coordinate system's origin set at the center of A -facet.

$$\frac{\partial^2 T}{\partial x^2} + \frac{\partial^2 T}{\partial y^2} + \frac{\partial^2 T}{\partial z^2} = -\frac{Q(x, y, z)}{K_c} \quad (9)$$

Here, K_c represents thermal conductivity of the gain material, and $Q(x, y, z)$ denotes the heat source density within the resonator. The internal heat sources in the resonator arise from non-radiative transitions during operation. Distinct from direct heating, the conversion of external input P_{abs} into thermal energy is attributed to the difference between the pump laser power P_{pump} and the output laser power, as delineated in Eq. (10),

$$P_{abs} = (P_{pump} - P_{th}) \times (1 - \eta_{slope}) + P_{th} \quad (10)$$

where P_{th} is the laser threshold power, and η_{slope} is the laser slope efficiency. The heat source density can be expressed as Eq. (11),

$$Q(x, y, z) = \frac{2P_{abs}}{\pi\omega_p^2} \times \exp\left(\frac{-2(x^2 + y^2)}{\omega_p^2} - \alpha z\right) \quad (11)$$

where ω_p is the Gaussian radius of the pump light (assuming constant radius during propagation) and α is the absorption coefficient of the resonator.

The temperature distribution within the resonator under steady-state conditions was analyzed using FEM. Fig. 7 presents the thermal field within the resonator, temperature distribution of the axial section along leg AB and the A -facet, under a pump power of 1000 mW.

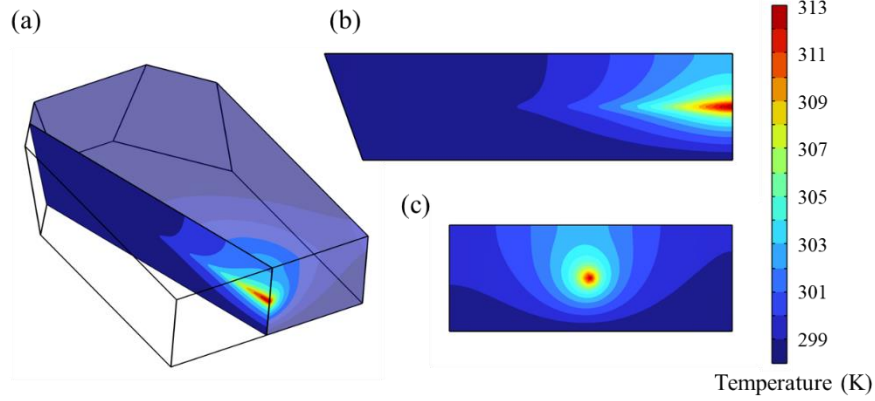


Fig. 7. (a) Temperature distribution within NPRO. (b) Temperature distribution of axial section along leg AB . (c) Temperature distribution of A -facet. In the simulations, $P_{th}=100$ mW, $\eta_{slope} = 60\%$, $\omega_p = 0.1$ mm, $\alpha = 4.6$ cm⁻¹. The temperature control of the resonator base is set to 25 °C. Other surfaces dissipate heat through air convection.

Upon transmission through the resonator illustrated in Fig. 7, the beam undergoes focusing. By employing ray-tracing-method as shown in Fig. 8(a), we can calculate the equivalent focal length of thermal-lens induced by the heterogeneous temperature distribution within the resonator. By comparing the Gaussian beam radius ($1/e^2$) of the beam profile at the A -facet before (0.2 mm) and after (0.19 mm) the thermal field effect, the equivalent focal length of the thermal-lens at a pump power of 1000 mW is calculated to be approximately 1352 mm, as demonstrated in Fig. 8(b). This is achieved by analyzing the alterations in the spot size and shape of the output beam after it traverses the resonator in one round-trip. This analysis provides critical insights into the optical path modifications induced by thermal effects within the gain medium. By combining thermodynamic simulations with ray-tracing-method, we can calculate the equivalent focal length of the thermal-lens with varying pump power, as shown in Fig. 8(c). One can see the equivalent focal length decrease from 6.35 m to 0.25 m with pump power increased from 0.2 W to 10.2 W.

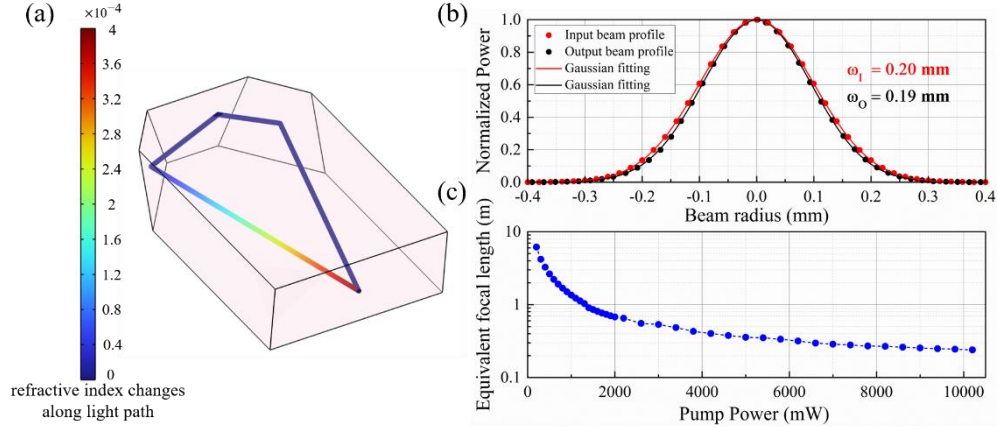


Fig. 8. (a) Equivalent focal length calculation using tracing ray in the resonator. The color bar shows the refractive index changes along the light path under 1000 mW pump power. (b) Normalized power distribution versus beam radius. Red dots and Gaussian fitting: input transmitting beam profile without pump laser heating; Black dots and Gaussian fitting: output transmitting beam profile with pump laser heating. The beam radius ω_1 and ω_0 at $1/e^2$ of the beam power are given by the fittings. (c) Equivalent focal length of the thermal-lenses under different pump power.

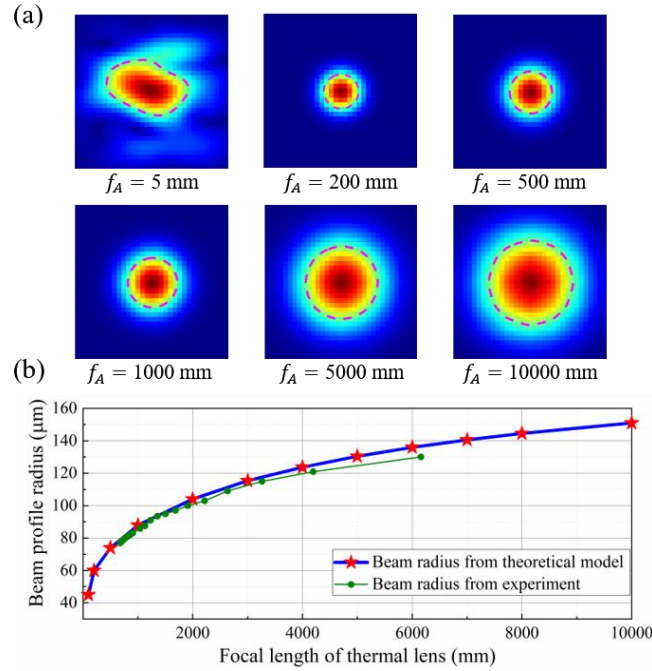


Fig. 9. (a) Beam profiles at point S with different focal length of thermal-lens. (b) Beam profile radius of different thermal-lenses tested from theoretical model and experiment. In the simulations, $AE=10.5$ mm, $CE=1.5$ mm, $\beta=90^\circ$, $\theta_A=15^\circ$, $f_B=10^5$ m.

We utilized the theoretical model presented in Section 3 to calculate the impact of thermal-lens effects on the output beam profiles, which are shown in Fig. 9. Our simulations indicate that the beam field has good symmetry under pump power of 12.0 W, and the asymmetry arises after the pump powers are beyond 12.0 W, where the f_A is lower than 100 mm. In practical applications, this situation may lead to non-resonance within the laser cavity. For high-power

pumped NPRO laser, to mitigate severe thermal-lens effects, gradient doping or using a negative curvature lens at the A-facet can be employed. Furthermore, a slighter thermal effect correlates with a larger beam profile on the output surface, which is consistent with general expectations.

In experimental measurements, it is not possible to directly measure the beam profile at A-facet of NPRO. To validate the simulation results, we measured the beam radius of output laser and its divergence angle from the NPRO, which enables us to resolve the beam radius near A-facet. The schematic of the experimental setup is illustrated in Fig. 10. The pump source is a multimode laser diode with fiber-pigtail output, which provides a maximum pump power of 2 W at 808 nm. The pump beam from the laser diode is injected to the Nd:YAG NPRO by a single focus-lens. A pair of neodymium magnets generates sufficient magnetic field for unidirectional emission at 1064 nm [36]. Temperature stabilization for both the laser diode and the NPRO is provided by thermoelectric cooler modules. The output laser beam profile is measured using a CMOS camera (Thorlabs, BC207VIS).

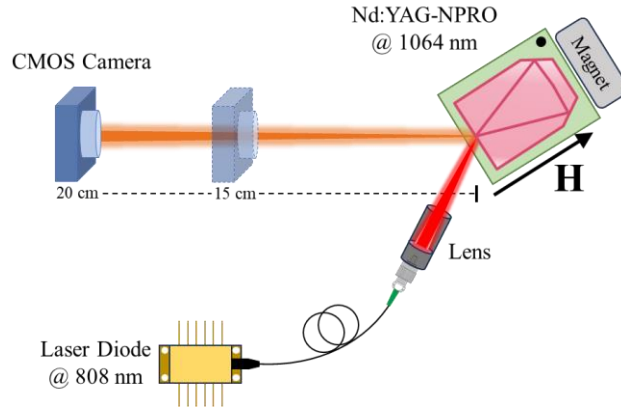


Fig. 10. The schematic of the experimental setup for beam profile measurements.

We varied the pump power and measured the radius of the output beam at distances of 15 cm and 20 cm from A-facet of the NPRO. These data are used to approximately calculate the divergence angle of the output beam by Eq. (12). The results are shown in Fig. 11, where the pump power increases from 200 mW to 2000 mW, and the divergence angle of the output laser also increases significantly from 0.16° to 0.40° .

$$\text{Divergence Angle} = \arctan\left(\frac{R_{20\text{ cm}} - R_{15\text{ cm}}}{5\text{ cm}}\right) \quad (12)$$

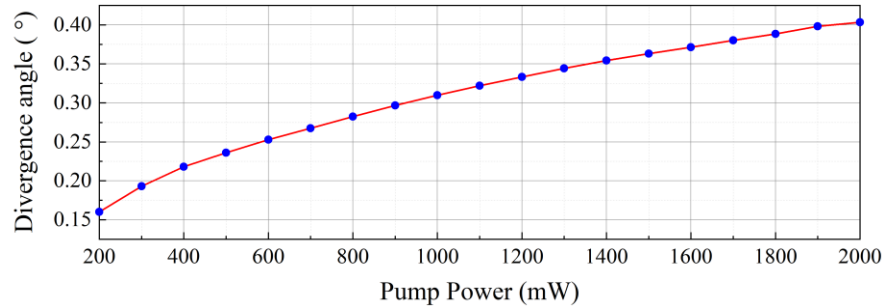


Fig. 11. Divergence angles of the output beam measured under different pump power.

Using the divergence angle of the output laser and the beam radius at the distance of 15 cm or 20 cm, we can calculate the beam radius at the A-facet corresponding to different pump powers under the effect of thermal-lens, as shown in Fig. 9(b) by the green dots. They show

good match with theoretical simulations with slight discrepancies at large beam profile radius (corresponding to slight thermal-lens effect at low pump power). We attribute this to higher calculation errors of the beam radius under lower pump powers. Although our experiments were limited by the maximum output power of the pump diode, preventing us from measuring results beyond 2 W, the agreement between the available experimental data and simulation calculations allows us to reasonably speculate that the results under high pump-power conditions (> 600 mW) will closely align with those predicted by the simulations. The integration of the output light field model presented in Section 3 with the thermal-lens calculation model in this Section provides valuable guidance for the design of high power NPRO lasers. This model will be utilized to predict the thermal-lens effects under high pump-power conditions and to mitigate the occurrences that lead to output laser distortions.

5. Conclusions

In conclusion, we have developed a transfer matrix for the nonplanar ring laser loop in monolithic NPRO and calculated the output laser beam profile using FEM to discretize the cavity mirrors. Our analysis of various geometrical parameters revealed that the lengths of AE and CE can control the size of the beam profile, while the laser incidence angle influences the symmetry of the beam profile. Additionally, we focused on the effects of thermal-lens within the monolithic NPRO. By combining optical simulations with solid-state heat transfer calculations, we obtained the temperature distribution within the cavity and calculated the equivalent-focal-length of the thermal-lens. Furthermore, we integrated these results with theoretical model of the output beam profile to assess the effects of different thermal-lenses on the beam profiles, which are well examined by experiments. Our comprehensive analysis on the mode patterns and thermal-lens effect will facilitate the design of monolithic NPROs used for single-frequency lasers and laser gyroscopes, and help to improve their performances in various fields, including but not limited to, fundamental research, precision metrology, high-end industry, and deep-space exploration.

Funding. National Natural Science Foundation of China (12404489); Fundamental Research Funds for the Central Universities, Sun Yat-sen University (24QNPY162); National Key Research and Development Program of China (2020YFC2200200); Major Projects of Basic and Applied Basic Research in Guangdong Province (2019B030302001).

Acknowledgments.

Disclosures. The authors declare no competing interests.

Data availability. Data underlying the results presented in this paper are not publicly available at this time but may be obtained from the authors upon reasonable request.

References

1. A. R. Clobes and M. J. Brienza, "Single-frequency traveling-wave Nd:YAG laser," *Appl. Phys. Lett.* **21**, 265–267 (1972).
2. T. A. Dorschner, "Nonplanar Rings for Laser Gyroscopes," in E. L. Moore and O. G. Ramer, eds. (1983), pp. 192–202.
3. W. W. Chow, J. Gea-Banacloche, L. M. Pedrotti, V. E. Sanders, W. Schleich, and M. O. Scully, "The ring laser gyro," *Rev. Mod. Phys.* **57**, 61–104 (1985).
4. M. Vallet, N. H. Tran, P. Tanguy, A. Le Floch, and F. Bretenaker, "Ring-laser gyro with spatially resolved eigenstates," *Opt. Lett.* **19**, 1219 (1994).
5. K. Wang, L. Feng, J. Wang, and M. Lei, "Alternative method for design and optimization of the ring resonator used in micro-optic gyro," *Appl. Opt.* **52**, 1481 (2013).
6. T. J. Kane and R. L. Byer, "Monolithic, unidirectional single-mode Nd:YAG ring laser," *Opt. Lett.* **10**, 65 (1985).
7. G. M. Harry and the LIGO Scientific Collaboration, "Advanced LIGO: the next generation of gravitational wave detectors," *Class. Quantum Gravity* **27**, 084006 (2010).

8. B. S. Sheard, G. Heinzel, K. Danzmann, D. A. Shaddock, W. M. Klipstein, and W. M. Folkner, "Intersatellite laser ranging instrument for the GRACE follow-on mission," *J. Geod.* **86**, 1083–1095 (2012).
9. M. Dubois, K. C. Burr, and T. E. Drake, "Laser phase noise reduction for industrial interferometric applications," *Appl. Opt.* **43**, 4399 (2004).
10. G.-W. Sun, D.-J. Chen, G.-F. Xin, H.-W. Cai, W.-B. Chen, and on behalf of The Taiji Scientific Collaboration, "High stability laser source for Taiji-1 satellite," *Int. J. Mod. Phys. A* **36**, 2140006 (2021).
11. Y. Luo, H. Li, Y. Li, Z. Zhan, C. Huang, J. Lai, and H.-C. Yeh, "Prototype of a monolithic cavity-based ultrastable optical reference for space applications," *Appl. Opt.* **60**, 2877 (2021).
12. G. Lin and Y. K. Chembo, "(INVITED) Monolithic total internal reflection resonators for applications in photonics," *Opt. Mater. X* **2**, 100017 (2019).
13. J. Li, W. Fan, J. Xu, Z. Huang, J. Luo, X. Yu, Y. Hu, Q. Yang, C. Guo, and H.-C. Yeh, "Low-noise high-power dual-frequency MOPA laser with an NPRO seed," *Opt. Express* **33**, 4889 (2025).
14. D. Liu, C. Guo, C. Ma, W. Fan, X. Gong, Z. Zhang, W. Li, J. Xu, K. Liu, and H.-C. Yeh, "All-solid-state miniature laser gyroscope based on a single monolithic non-planar ring oscillator," *Photonics Res.* (2025). DOI 10.1364/PRJ.543856
15. F. Wellmann, N. Bode, P. Wessels, L. Overmeyer, J. Neumann, B. Willke, and D. Kracht, "Low noise 400 W coherently combined single frequency laser beam for next generation gravitational wave detectors," *Opt. Express* **29**, 10140 (2021).
16. P. Kwee, C. Bogan, K. Danzmann, M. Frede, H. Kim, P. King, J. Pödl, O. Puncken, R. L. Savage, F. Seifert, P. Wessels, L. Winkelmann, and B. Willke, "Stabilized high-power laser system for the gravitational wave detector advanced LIGO," *Opt. Express* **20**, 10617 (2012).
17. Z. Li, H. Duan, X. Huang, M. Ming, P. Liu, S. Zou, G. Wang, X. Zhang, M. Yang, B. Cao, Q. Liu, S. Yang, L. Tu, and H. Yeh, "Design and performance test of the spaceborne laser in the TianQin-1 mission," *Opt. Laser Technol.* **141**, 107155 (2021).
18. Q. Yin, H. Lu, and K. Peng, "Investigation of the thermal lens effect of the TGG crystal in high-power frequency-doubled laser with single frequency operation," *Opt. Express* **23**, 4981 (2015).
19. I. Freitag, A. Tünnermann, and H. Welling, "Power scaling of diode-pumped monolithic Nd:YAG lasers to output powers of several watts," *Opt. Commun.* **115**, 511–515 (1995).
20. M. Shayganmanesh, M. H. Daemi, Zh. Osgoui, S. Radmard, and S. Sh. Kazemi, "Measurement of thermal lensing effects in high power thin disk laser," *Opt. Laser Technol.* **44**, 2292–2296 (2012).
21. F. Wu, L. Yu, J. Lu, W. Li, Y. Xu, and Y. Leng, "Suppression of thermal lens effect in high-pulse-energy Ti:sapphire amplifiers," *Opt. Laser Technol.* **87**, 94–98 (2017).
22. Z. Li, C. Shi, R. Fang, Q. Feng, B. Xiao, H. Xu, and Z. Cai, "Power scaling of diode-pumped Pr:YLF lasers in the 910 nm spectral range," *Opt. Laser Technol.* **153**, 108198 (2022).
23. X. Zhao, G. Shi, N. Deng, Y. Qu, J. Yuan, L. Du, W. Hu, Z. Zhang, and H. Wang, "Thermal effect suppression of end-pumped rod-like Nd:YAG laser crystal utilizing the diamond cap strategy," *Opt. Laser Technol.* **181**, 111932 (2025).
24. E. J. Zang, J. Cao, M. Zhong, C. Li, N. Shen, D. Hong, L. Cui, Z. Zhu, and A. Liu, "Relaxed alignment tolerance of monolithic ring lasers," *Appl. Opt.* **41**, 7012 (2002).
25. J. Yuan, X. Long, L. Liang, B. Zhang, F. Wang, and H. Zhao, "Nonplanar ring resonator modes: generalized Gaussian beams," *Appl. Opt.* **46**, 2980 (2007).
26. J. Yuan and X. Long, "Optical-axis perturbation in nonplanar ring resonators," *Opt. Commun.* **281**, 1204–1210 (2008).
27. W. R. Trutna, D. K. Donald, and M. Nazarathy, "Unidirectional diode-laser-pumped Nd:YAG ring laser with a small magnetic field," *Opt. Lett.* **12**, 248 (1987).
28. D. J. Ottaway, P. J. Veitch, M. W. Hamilton, C. Hollitt, D. Mudge, and J. Munch, "A compact injection-locked Nd:YAG laser for gravitational wave detection," *IEEE J. Quantum Electron.* **34**, 2006–2009 (1998).
29. H. Zimer and U. Wittrock, "16 W of single-mode output power from a novel power-scaling scheme for monolithic nonplanar ring lasers," *Opt. Lett.* **29**, 1635 (2004).
30. P. Burdack, T. Fox, M. Bode, and I. Freitag, "1 W of stable single-frequency output at 1.03 μm from a novel, monolithic, non-planar Yb:YAG ring laser operating at room temperature," *Opt. Express* **14**, 4363 (2006).
31. Q. Zhou, P. Gong, Y. Pan, Y. Zhou, S. Wu, and S. Qiu, "Numerical modeling of thermal lens effects in a nonplanar ring oscillator laser," *Appl. Phys. B* **131**, 24 (2025).
32. Y. V. Filatov, P. A. Pavlov, A. A. Velikoseltsev, and K. U. Schreiber, "Precision Angle Measurement Systems on the Basis of Ring Laser Gyro," *Sensors* **20**, 6930 (2020).
33. G. Zhou, R. Zhu, C. Ma, X. Gong, W. Fan, S. Zhou, J. Xu, C. Guo, and H.-C. Yeh, "Unidirectional operation criterion in monolithic nonplanar ring oscillators," *Opt. Lett.* **48**, 3047 (2023).
34. S. Schwartz, F. Guty, G. Feugnet, É. Loil, and J.-P. Pocholle, "Solid-state ring laser gyro behaving like its helium-neon counterpart at low rotation rates," *Opt. Lett.* **34**, 3884 (2009).
35. P. Vaity, J. Banerji, and R. P. Singh, "Measuring the topological charge of an optical vortex by using a tilted convex lens," *Phys. Lett. A* **377**, 1154–1156 (2013).
36. W. Fan, C. Ma, D. Liu, R. Zhu, G. Zhou, X. Gong, S. Zhou, J. Xu, W. Yuan, C. Guo, and H.-C. Yeh, "Dual-frequency fundamental-mode NPRO laser for low-noise microwave generation," *Opt. Express* **31**, 13402 (2023).